

# A numerical study of flow boiling in a microchannel using the local front reconstruction method

**Citation for published version (APA):**

Rajkotwala, A., Boer, L., Peters, E. A. J. F., van der Geld, C. W. M., Kuerten, J. G. M., Kuipers, J. A. M., & Baltussen, M. W. (2022). A numerical study of flow boiling in a microchannel using the local front reconstruction method. *AICHE Journal*, 68(4), Article e17598. <https://doi.org/10.1002/aic.17598>

**DOI:**

[10.1002/aic.17598](https://doi.org/10.1002/aic.17598)

**Document status and date:**

Published: 01/04/2022

**Document Version:**

Publisher's PDF, also known as Version of Record (includes final page, issue and volume numbers)

**Please check the document version of this publication:**

- A submitted manuscript is the version of the article upon submission and before peer-review. There can be important differences between the submitted version and the official published version of record. People interested in the research are advised to contact the author for the final version of the publication, or visit the DOI to the publisher's website.
- The final author version and the galley proof are versions of the publication after peer review.
- The final published version features the final layout of the paper including the volume, issue and page numbers.

[Link to publication](#)

**General rights**

Copyright and moral rights for the publications made accessible in the public portal are retained by the authors and/or other copyright owners and it is a condition of accessing publications that users recognise and abide by the legal requirements associated with these rights.

- Users may download and print one copy of any publication from the public portal for the purpose of private study or research.
- You may not further distribute the material or use it for any profit-making activity or commercial gain
- You may freely distribute the URL identifying the publication in the public portal.

If the publication is distributed under the terms of Article 25fa of the Dutch Copyright Act, indicated by the "Taverne" license above, please follow below link for the End User Agreement:

[www.tue.nl/taverne](http://www.tue.nl/taverne)



**Take down policy**

If you believe that this document breaches copyright please contact us at:

[openaccess@tue.nl](mailto:openaccess@tue.nl)

providing details and we will investigate your claim.

# A numerical study of flow boiling in a microchannel using the local front reconstruction method

Adnan H. Rajkotwala<sup>1</sup> | Leander L Boer<sup>2</sup> | E. A. J. F. (Frank) Peters<sup>1</sup>  |  
Cees W. M. van der Geld<sup>2</sup> | J. G. M. (Hans) Kuerten<sup>3</sup> | J. A. M. (Hans) Kuipers<sup>1</sup> |  
Maïke W. Baltussen<sup>1</sup> 

<sup>1</sup>Multiphase Reactors Group, Department of Chemical Engineering and Chemistry, Eindhoven University of Technology, Eindhoven, The Netherlands

<sup>2</sup>Interfaces with Mass Transfer Group, Department of Chemical Engineering and Chemistry, Eindhoven University of Technology, Eindhoven, The Netherlands

<sup>3</sup>Power and Flow Group, Department of Mechanical Engineering, Eindhoven University of Technology, Eindhoven, The Netherlands

## Correspondence

Maïke W. Baltussen, Department of Chemical Engineering and Chemistry, Eindhoven University of Technology, P.O. Box 513, Eindhoven, 5612 AZ, The Netherlands.  
Email: m.w.baltussen@tue.nl

## Funding information

Stichting voor de Technische Wetenschappen, Grant/Award Numbers: Open Technologieprogramma, grant number, 13781; Technology Foundation STW; Netherlands Organisation for Scientific Research

## Abstract

The rapid advances in performance and miniaturization of electronic devices require a cooling technology that can remove the produced heat at a high rate with small temperature variations, as is obtained in flow boiling. To obtain insight in flow boiling, we performed numerical simulations in a 200  $\mu\text{m}$  square microchannel using the local front reconstruction method. Besides validation with literature results, a parametric study shows an increasing heat removal rate and bubble growth rate with increasing wall temperature, liquid mass density, and liquid heat capacity and decreasing inlet velocity indicating the importance of phase change compared to convective transport. Finally, the heat transfer in the liquid film is studied using a Nusselt number defined with the film thickness, which is comparable to Nusselt number for falling films on hot surfaces. It is observed that convective effects are more pronounced at the bubble rear compared to the bubble front.

## KEYWORDS

flow boiling, front tracking, local front reconstruction method, microchannel, numerical simulation, sharp interface approach

## 1 | INTRODUCTION

Many miniaturized devices, for example, computational processing units (CPUs), graphical processing units (GPUs), memory cards, data storage devices, semiconductor devices, laser diode arrays, and proton exchange membrane fuel cells, require high heat transfer rates over a relatively small area.<sup>1</sup> For cooling these devices, flow boiling is one of the promising technologies. This two-phase cooling method has several advantages over conventional cooling strategies: a lower mass flow rate of the coolant due to the high energy uptake by the latent heat of vaporization, a lower pressure drop due to the lower required mass flow rate, lower temperature gradients due to saturated flow conditions and an increase of the heat transfer coefficient with

increasing heat flux.<sup>2</sup> The heat transfer associated with the boiling process is further enhanced by the relatively large liquid–vapor interfacial area offered by the geometry of the microchannel.<sup>3</sup> Due to the dominant effect of the capillary forces in microchannels, dispersed bubbly flow is quickly suppressed at low vapor qualities by the rapid expansion of the nucleating bubbles resulting in slug flow as the dominant flow regime.<sup>4</sup>

The slug flow regime is characterized by the presence of elongated bubbles, which trap a thin liquid film against the channel wall, alternated by liquid pockets and is considered to be the flow regime enabling efficient heat transfer.<sup>4</sup> Due to the importance of the slug flow regime in microchannels, we focus in this article on the growth of a vapor bubble to form a vapor slug. Over the past few decades,

This is an open access article under the terms of the Creative Commons Attribution License, which permits use, distribution and reproduction in any medium, provided the original work is properly cited.

© 2022 The Authors. *AIChE Journal* published by Wiley Periodicals LLC on behalf of American Institute of Chemical Engineers.

many experimental investigations have been carried out on flow boiling in microchannels. These studies led to the development of theoretical models for the prediction of the pressure drop and the heat transfer coefficient for flow boiling in microchannels. Detailed reviews of experimental studies and analytical models of microchannel flow boiling are available in literature.<sup>5–9</sup> These reviews compare various experimental data sets and evaluate the available theoretical models against these data sets. The main conclusions are that the experimental outcomes are often contradictory and that the available analytical models do not provide satisfactory predictions.<sup>10</sup> Thus, the lack of agreement on the heat transfer performance trends combined with the limitations of the experimental measurement techniques to probe into the local flow and heat transfer phenomena poses a serious limitation to advance the fundamental understanding.

Unlike experiments, numerical simulations can provide detailed information on the local hydrodynamics and heat transfer of boiling flows in microchannels and thus have become an important research tool. Previously, Mukherjee and Kandlikar<sup>11</sup> carried out 3D simulations of vapor bubble growth during flow boiling of water in a 0.2 mm square microchannel using a Level Set (LS) method. They assumed the vapor phase to remain at a saturation temperature of 373.15 K. The simulations were initiated with a vapor bubble placed in the center of the channel cross-section. They reported a rapid increase in the growth rate of the bubble when it filled the channel cross-section. This increase in growth rate was attributed to evaporation of the thin liquid film that is trapped between the bubble and channel walls. The authors qualitatively compared bubble shape evolution with experimental data and observed a good agreement. A quantitative comparison was not performed because the physical parameters of the experiments were not replicated in the simulations. The authors found that the bubble growth rate increases with increasing superheat, while gravity has a negligible influence, as expected. Surprisingly, the vapor patch formation at the walls was not observed at higher liquid superheat. The authors reasoned that lack of sufficient time for the thin layer to start boiling at higher superheat prevented formation of such vapor patches.

Using the same numerical model and physical parameters as in Mukherjee and Kandlikar,<sup>11</sup> Mukherjee et al.<sup>12</sup> performed 3D transient simulations for vapor bubble growth attached to a wall in a microchannel. The authors studied the effect of the wall superheat, the liquid Reynolds number, the surface tension, and the contact angle between the liquid–vapor interface and the wall on bubble growth and the heat transfer from the heated wall of the channel. The bubble growth rate and heat transfer rate from the wall were shown to increase with wall superheat and a minor variation was observed with the inlet liquid Reynolds number and surface tension (within the range considered in their study). An interesting outcome of the study was that a very high bubble growth rate was observed at a contact angle of 20° compared to angles of 40°, 60°, and 80°. This was attributed to boiling in the thin film. A higher contact angle resulted in a larger wall area exposed to the vapor and therefore, in a lower wall heat transfer rate. A limitation in their parametric study was that the simulations were initialized with zero liquid velocity deviating from practical situations where bubble formation in a steady laminar flow prevails.

Lee and Son<sup>13</sup> performed 3D simulation of nucleation and growth of a water vapor bubble in rectangular microchannels of various sizes using the LS method. The method was coupled to a microlayer model to account for evaporative mass transfer in the microlayer between the bubble and the bottom wall (near the bubble wall contact location). The authors showed that the bubble growth rate (and hence heat transfer rate from the wall) in a microchannel (0.4 mm) is significantly higher than in a larger channel (3 mm). No thin film was formed in the larger channel, thus indicating the importance of the thin film in heat transfer during flow boiling in a microchannel. In addition, the authors showed that the heat transfer rate from the wall increased with decreasing contact angle, which is in agreement with the results of Mukherjee et al.<sup>12</sup>

Zu et al.<sup>14</sup> simulated nucleation and growth of a bubble in a 0.38 mm height rectangular microchannel using the Volume of Fluid (VOF) method in ANSYS Fluent. The authors used the concept of “pseudo-nucleate boiling” which separated the bubble evolution into two stages. In the first stage, the bubble growth on the wall and bubble lift-off are controlled to match the experimental data. After bubble detachment from the wall, the bubble growth rate is driven by a constant heat flux equal to the average wall heat flux. The simulation results agree well with the experiments, which is not surprising as the initial growth and lift-off were controlled by experimental data. In addition, the assumption in the second stage that the bubble evaporation rate is driven by average wall heat flux puts a limitation to the generality of their CFD model.

Zhuan and Wang<sup>15</sup> studied flow pattern transitions in a 0.5 mm diameter circular microchannel using the VOF method. Similar to Zu et al.,<sup>14</sup> the bubble evaporation was treated in two different stages: nucleation bubble growth and slug bubble growth. In the first stage, an analytical model for the bubble growth rate was used and for the second stage an energy jump condition was used to calculate the evaporated mass flux. In their study, the effect of bubble lift-off size, heat flux, mass velocity, frequency of bubble generation, and fluid properties on flow pattern transition were studied.

Magnini et al.<sup>4</sup> studied the hydrodynamics and heat transfer of an elongated bubble during flow boiling in a 0.5 mm diameter circular microchannel by performing 2D axisymmetric simulations using the VOF method in ANSYS Fluent. Because the authors used an axisymmetric model, low wall heat fluxes, high inlet mass flow rates, and refrigerants as working fluids, relatively thick films were found between the bubble and the wall, which enabled them to completely resolve the thin film in their simulations. A Taylor bubble is introduced in an adiabatic entry region to allow it to reach a hydrodynamic steady state before it enters the heated region. When the bubble comes into contact with the superheated thermal boundary layer, it starts to grow rapidly, resulting in the acceleration of the bubble nose along the channel length and increasing heat transfer rate from the wall. The authors also observed that the heat transfer coefficient monotonically increases with decreasing average film thickness, indicating the importance of thin film evaporation for the overall wall heat transfer.

Using the same numerical model, the authors extended the above work to simulate multiple elongated bubbles and investigated the influence of bubble interaction on flow boiling heat transfer in microchannels.<sup>16</sup> Magnini and Thome<sup>17</sup> utilized the numerical results from

these studies to improve the two zone analytical model of Jacobi and Thome.<sup>18</sup> Magnini and Thome<sup>3</sup> further extended their single bubble work<sup>4</sup> by carrying out simulations for varying operating conditions (wall heat flux, inlet mass flux, and bubble generation frequency), different operating fluids, and channel diameters. Their study was concluded with a dimensional analysis identifying the nondimensional numbers which are important for the hydrodynamics and heat transfer of microchannel slug flow boiling.

Recently, Ferrari et al.<sup>19</sup> carried out simulations of slug flow boiling in square microchannel using the VOF method in OpenFOAM and compared the bubble dynamics and heat transfer to that of slug flow boiling in a circular microchannel. The authors reported that for a square microchannel, the bubble shape loses axisymmetry below a critical capillary number leading to varying liquid film thickness along the perimeter of the channel cross-section. The nonaxisymmetric bubble shape gave rise to transversal draining flows that make the liquid film thinner at the rear of the bubble.

As shown in the previous literature review, the existing numerical studies have been performed with front capturing methods only. Both used methods have their intrinsic limitations, that is, LS methods have issues with mass conservation, while the VOF approach faces limitations to accurately account for surface tension forces.<sup>4</sup> Flows in microchannels are dominated by capillary effects and thus it is important to use a numerical method that allows for an accurate and robust surface tension force calculation. These methods are inherently better suited to accurately calculate the surface tension because the interfaces are directly tracked.<sup>20–23</sup> Therefore, in this study, we use a hybrid front tracking method without connectivity, the local front reconstruction method (LFRM)<sup>23</sup> to study flow boiling in a square microchannel.

The LFRM can easily handle complex topological changes like droplet collisions and merging and can accurately capture the interface dynamics while using relatively coarse grids compared to front capturing methods.<sup>23</sup> We have extended the LFRM to include phase transition using a sharp interface approach for the energy equation.<sup>24</sup> The extended method has been verified against analytical solutions for standard 1D and 3D tests and validated against experimental data for 3D bubble rise and growth in a supersaturated liquid. The details of the implementation along with verification and validation results can be found in Rajkotwala et al.<sup>24</sup> Therefore, only a summary of the implementation is given in Section 2. In this article, we further extend verification and validation of the LFRM model by comparing simulations of a Taylor bubble rise in a vertical channel with experiments (Section 3). We also compare the simulations of a 3D bubble growth in supersaturated liquid under zero gravity condition using real water-steam properties with the analytical solution (Section 4).

In Section 5, the simulation of growth of a single vapor bubble during flow boiling in a microchannel is performed using LFRM and compared to the simulation results of Mukherjee and Kandlikar.<sup>11</sup> A parametric study is performed in Section 6 to characterize the influence of various thermal and hydraulic parameters like wall superheat, inlet velocity, liquid mass density, and liquid heat capacity on the growth of the vapor slug and net heat transfer from the wall during flow boiling. In Section 7, the heat transfer in the liquid film is studied in detail, which is believed to be the

driving force for the vapor bubble growth during microchannel flow boiling. Even though these are state-of-the-art computations, it should be noted that there might still be some grid dependency in the simulation results, because of the limited grid resolution in the thinnest parts of the liquid film. Finally, conclusions are presented in Section 8.

## 2 | NUMERICAL MODEL

### 2.1 | Governing equations

In this study, we will use the LFRM detailed in Rajkotwala et al.<sup>24</sup> Therefore, only the main characteristics of the method are given here. The flow equations for velocity  $\mathbf{u}$  are solved by a one fluid formulation with suitable liquid–vapor equilibrium conditions at the interface. Although both phases are assumed to be incompressible, the expansion due to phase change is incorporated by modifying the divergence-free velocity field condition at the interface. The energy equation is treated with a sharp interface approach. In this approach, the thermal properties are not volume-averaged near the interface and the temperature at the interface is set as a boundary condition to the saturation temperature. For standard variables that appear in the equations below, we adhere to common choices of symbols like mass density  $\rho$ , temperature  $T$ , thermal conductivity  $\lambda$ , viscosity  $\mu$ , surface tension  $\sigma$ , isobaric heat capacity  $C_p$  etc. The subscripts l and g refer to liquid and gas. The governing equations are as follows:

#### 2.1.1 | Mass conservation equation

$$\nabla \cdot \mathbf{u} = \left( \frac{1}{\rho_g} - \frac{1}{\rho_l} \right) \int_{A_f} \delta(x - x_f) \dot{m} dA_f, \quad (1)$$

where  $\dot{m}$  is the interfacial mass flux, which is calculated from the heat flux  $\dot{q}$  at the interface using the simplified energy jump condition:

$$\dot{m} h_{lg} = \dot{q} = \lambda_g \frac{\partial T}{\partial n_g} \Big|_g - \lambda_l \frac{\partial T}{\partial n_l} \Big|_l, \quad (2)$$

where  $h_{lg}$  is the latent heat measured at the equilibrium saturation temperature  $T_{\text{sat}}(P)$ , corresponding to the reference ambient system pressure.

#### 2.1.2 | Momentum conservation equation

$$\rho \frac{\partial \mathbf{u}}{\partial t} + \rho \{ \nabla \cdot (\mathbf{u}\mathbf{u}) - \mathbf{u}(\nabla \cdot \mathbf{u}) \} = -\nabla p + \rho \mathbf{g} + \nabla \cdot \boldsymbol{\tau} + \mathbf{F}_\sigma, \quad (3)$$

where  $\boldsymbol{\tau} = \mu(\nabla \mathbf{u} + \nabla \mathbf{u}^T)$  is the viscous stress tensor and  $\mathbf{F}_\sigma$  is the volumetric surface tension force density. The convection term is

formulated in a semiconservative form to enable discretization by a total variation diminishing (TVD) scheme.

### 2.1.3 | Energy conservation equation

$$\rho C_p \frac{\partial T}{\partial t} + \rho C_p \{\nabla \cdot (\mathbf{u}T) - T(\nabla \cdot \mathbf{u})\} = \nabla \cdot (\lambda \nabla T). \quad (4)$$

Note that the viscous heating and pressure effects are neglected. The temperature of the interface is assumed to be the saturation temperature ( $T_{\text{sat}}$ ) and is imposed as a boundary condition using a sharp interface approach. Thus, an interfacial heat source term representing the latent heat is absent from the energy Equation 4.

## 2.2 | Interface treatment

The interface is represented by a surface mesh of triangular elements. This surface mesh enables advection of the interface and calculation of local phase fractions and surface tension force. The volumetric surface tension force density  $\mathbf{F}_\sigma = \sigma \int_{A_f} \delta(\mathbf{x} - \mathbf{x}_f) \kappa_f \mathbf{n}_f dA_f$ , with  $\kappa_f$  the local curvature, is calculated using the hybrid method of Shin et al.<sup>25</sup>

A vertex of the surface mesh with position  $\mathbf{x}_f$  is advected using the following equation:

$$\frac{d\mathbf{x}_f}{dt} = u_n \mathbf{n}_f, \quad (5)$$

where  $u_n$  is the normal interface velocity given by

$$u_n = \mathbf{u} \cdot \mathbf{n}_f - \frac{\dot{m}}{2} \left( \frac{1}{\rho_l} + \frac{1}{\rho_g} \right). \quad (6)$$

The normal interface velocity in the above equation has two components: the first term due to fluid advection and the second term due to phase change. The advection of the Lagrangian points leads to a decrease of the interface mesh quality. Thus, it is required to reconstruct the interface at regular time intervals. In this study, the interface is reconstructed using the modified LFRM.<sup>23,26</sup> The modified LFRM also accounts for the three phase contact line dynamics and details of this implementation can be found in Mirsandi et al.<sup>26</sup> In this study, a static contact angle is used when the bubble interface comes in contact with the wall in case of dryout.

## 2.3 | Numerical implementation of the fluid flow solver

The mass and momentum equations are spatially discretized on a staggered grid using a finite volume approach. A second order flux-delimited Barton scheme is used for the discretization of the

convection term and a second order central difference scheme is used for the discretization of the diffusion term.<sup>23</sup> The convection term is treated explicitly whereas the diffusion term is treated semi-implicitly. The explicit discretization of the convective term dictates the maximum allowable time-step size,  $\Delta t$ , through the Courant Friederich Lewis (CFL) criterion. The mass and momentum equations are solved in a coupled manner using a fractional step method.<sup>27</sup> In this method, a projection of velocity  $\mathbf{u}^n$  is calculated based on the Navier–Stokes equations:

$$\mathbf{u}^n = \mathbf{u}^n + \frac{\Delta t}{\rho^n} [-\rho \nabla \cdot (\mathbf{u}\mathbf{u}) - \nabla p + \rho \mathbf{g} - \nabla \cdot \boldsymbol{\tau} + \mathbf{F}_\sigma]^n. \quad (7)$$

The projected velocity is corrected using the pressure correction equation such that the resulting velocity field satisfies the modified continuity equation (Equation 1). The pressure correction,  $\delta p$ , follows from the solution of

$$\nabla \cdot \frac{\Delta t}{\rho} \nabla (\delta p) = \nabla \cdot \mathbf{u}^* - \nabla \cdot \mathbf{u}^{n+1}. \quad (8)$$

This Poisson equation is solved using an efficient and robust parallel Block-Incomplete Cholesky Conjugate Gradient (B-ICCG) solver.<sup>27</sup> It should be noted that the term  $\nabla \cdot \mathbf{u}^{n+1}$  is nonzero at the interface to account for expansion due to phase change.

The interfacial mass flux (required in Equation 1) is calculated on the surface mesh representing the interface using the normal probe method of Udaykumar et al.<sup>28</sup> as shown in Figure 1 and distributed to the Eulerian grid using a distribution function based on volume weighing. In the normal probe method, the normal derivatives in Equation 2 are approximated by using two probes (by means of a first order finite difference approximation).

$$\dot{m} = \frac{1}{h_{fg}} \frac{1}{\Delta n} [\lambda_g (T_g - T_{\text{sat}}) - \lambda_l (T_{\text{sat}} - T_l)], \quad (9)$$

where  $T_l$  and  $T_g$  are found by means of trilinear interpolation from the Eulerian grid to the probes and  $\Delta n$  is the probing distance taken equal to the grid size  $\Delta x$ .

## 2.4 | Numerical implementation of the energy solver

Once the flow field is solved and the interface is advected using the calculated flow field, the energy equation is solved using the updated velocity and physical properties. Similar to the mass and momentum equations, the energy equation is discretized using the finite volume method. The convective term is discretized with a second order flux-delimited Barton scheme,<sup>23</sup> whereas the conduction term is discretized with a second order central difference scheme. The convection term is treated explicitly whereas the conduction term is treated implicitly.



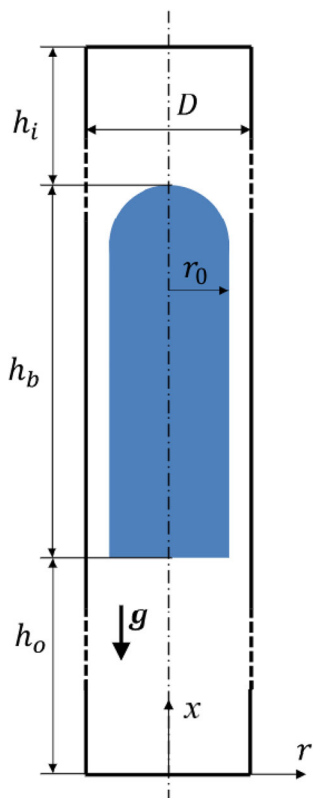


**FIGURE 3** Schematic of initial configuration of the Taylor bubble problem.<sup>31</sup>  $r_0 = 7$  mm,  $D = 19$  mm,  $h_b = 52.3$  mm,  $h_i \approx 1.5D$ , and  $h_o \approx 2D$

**TABLE 1** Gas and liquid properties for Taylor bubble problem

Property	Gas	Liquid
$\rho$ (kg/m <sup>3</sup> )	1.205	911
$\mu$ (Pa)	$1.827 \times 10^{-5}$	$8.4 \times 10^{-2}$
$\sigma$ (N/m)	0.0328	

simulations are continued until the Taylor bubble attains a constant terminal velocity.

### 3.2 | Results and discussion

The evolution of the bubble velocity with time is shown in Figure 4 for different grid resolutions. For all grid resolutions, the bubble has attained a constant rise velocity. There is a negligible difference between the medium and the fine grid results indicating grid convergence. The obtained bubble terminal velocities compare well with values obtained from experiments and other numerical studies as summarized in Table 2. The final shape of the Taylor bubble at steady state is shown in Figure 5.

Figure 6 shows the normalized axial velocity profile at several positions in the tube. Overall, there is a good agreement with the

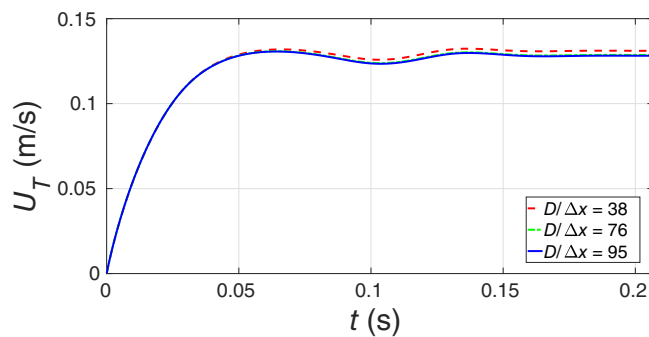


**FIGURE 4** Variation of the Taylor bubble velocity with time for different grid resolutions

**TABLE 2** Summary of calculated bubble terminal velocity and comparison with other works

Method	Literature	Terminal velocity (m/s)
LFRM ( $D/\Delta x = 38$ )	-	0.1311
LFRM ( $D/\Delta x = 76$ )	-	0.1287
LFRM ( $D/\Delta x = 95$ )	-	0.1282
Experiment	Bugg and Saad <sup>29</sup>	0.131
VOF	Ndinisa et al. <sup>30</sup>	0.140
LS	Gutiérrez et al. <sup>31</sup>	0.1286

Abbreviations: LFRM, local front reconstruction method; LS, level set; VOF, volume of fluid.

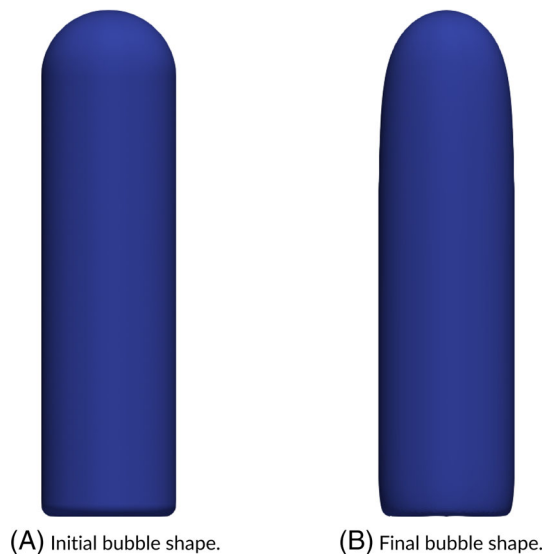


**FIGURE 5** Initial (A) and final (B) shape of the Taylor bubble at steady state for the grid resolution of  $D/\Delta x = 38$

experimental<sup>29</sup> and numerical results from literature.<sup>30,31</sup> Figure 6A reveals that the bubble perturbs the fluid in front of it, but the axial velocity decays swiftly. There exists a strong radial velocity component near the bubble nose, because the upward movement of the bubble causes the fluid to be pushed sideways. This creates a



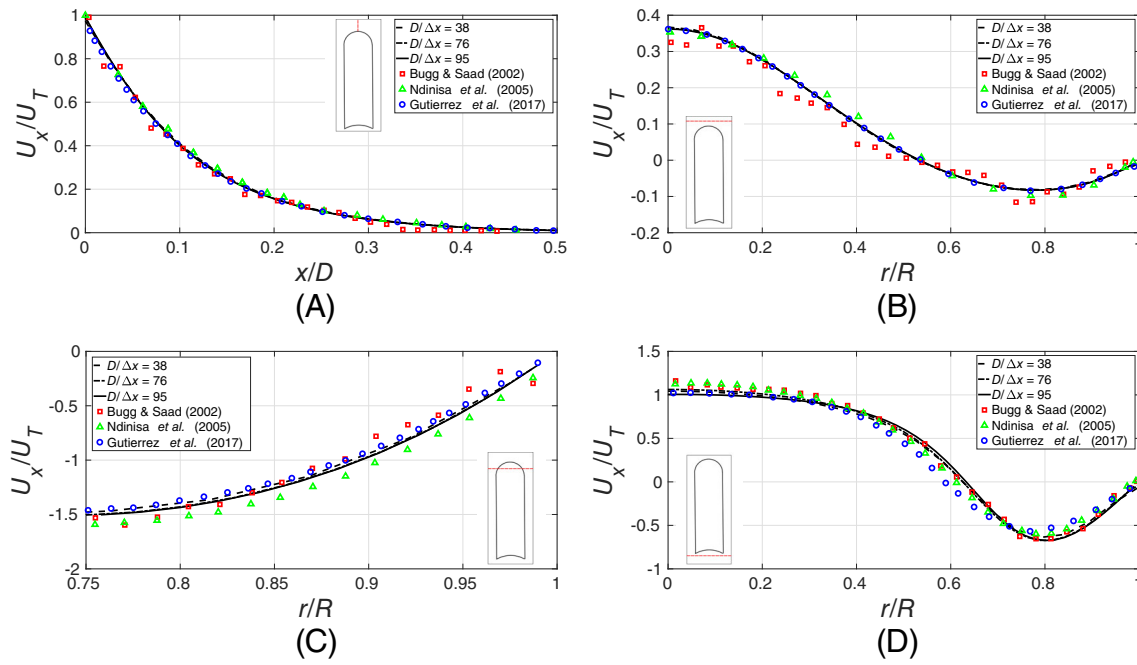


**FIGURE 6** Variation of normalized axial velocity (A) at the tube axis above the bubble nose (B) in the section at  $0.111D$  above the bubble nose and (C) in the developing film at  $0.504D$  below the bubble nose and (D) in the wake of the bubble

downward flow near the wall which is shown in Figure 6B. Figure 6C shows the normalized axial velocities in the developing film. The liquid in the film begins to fall due to gravity, inducing strong axial velocities in the film. The axial velocities are higher at the gas–liquid interface than at the wall due to the negligible shear stress at the gas–liquid interface. At the rear end of the bubble, the downward axial velocities near the wall are dramatically reduced, which can be seen in Figure 6D. Similar to the nose of the bubble, there is a strong radial velocity component that transfers the fluid from the wall toward the axis of the bubble.

#### 4 | 3D BUBBLE GROWTH UNDER ZERO GRAVITY CONDITION

The numerical model of phase transition used in this study has been thoroughly verified and validated in Rajkotwala et al.<sup>24</sup> However, the verification tests presented in Rajkotwala et al.<sup>24</sup> were carried out using artificial liquid–vapor properties. In this section, an extension of this verification and validation is made by simulating 3D bubble growth in supersaturated liquid using the physical properties of water and steam, with realistic viscosity and density ratios.

The detailed derivation of the analytical solution for this case can be found in literature.<sup>33,34</sup> The analytical solution for the bubble radius  $R$  as a function of time is given by

$$R = 2\beta \sqrt{\frac{\lambda_l}{\rho_l C_{pl}}} t, \quad (10)$$

where  $\lambda_l$ ,  $C_{pl}$ , and  $\rho_l$  are the thermal conductivity, the specific heat capacity, and the density of liquid, respectively, and  $\beta$  is the “growth constant.”  $\beta$  is obtained by solving the following implicit equation

$$\frac{\rho_l C_{pl} (T_\infty - T_{sat})}{\rho_g (h_{lg} + (C_{pl} - C_{pg})(T_\infty - T_{sat}))} = 2\beta^2 \int_0^1 \exp\left(-\beta^2 \left((1-\zeta)^{-2} - 2\left(1 - \frac{\rho_g}{\rho_l}\right)\zeta - 1\right)\right) d\zeta, \quad (11)$$

where  $C_{pg}$  and  $\rho_g$  are the specific heat capacity and the density of gas, respectively,  $h_{lg}$  is the latent heat and  $T_\infty$  is the super saturation temperature of the liquid.

The analytical solution for the temperature field at time  $t$  is given by

$$T = \begin{cases} T_\infty - 2\beta^2 \left( \frac{\rho_g (h_{lg} + (C_{pl} - C_{pg})(T_\infty - T_{sat}))}{\rho_l C_{pl}} \right) & r > R \\ \int_{1-\frac{r}{R}}^1 \exp\left(-\beta^2 \left((1-\zeta)^{-2} - 2\left(1 - \frac{\rho_g}{\rho_l}\right)\zeta - 1\right)\right) d\zeta & r > R \\ T_{sat} & r \leq R \end{cases} \quad (12)$$

#### 4.1 | Problem setup

As shown in Figure 7, a water vapor bubble of radius  $R_0 = 10 \mu\text{m}$  at saturation temperature  $T_{sat} = 373.15 \text{ K}$  is surrounded by liquid water at super saturation temperature with superheat  $\Delta T = 1 \text{ K}$ . The



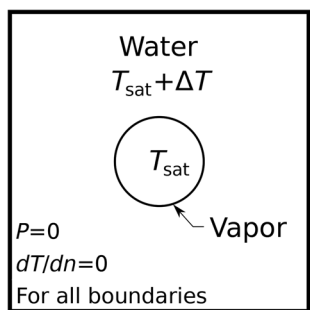


**FIGURE 7** Schematic of the 3D bubble growth problem

**TABLE 3** Thermophysical properties of water and water vapor

Property	Vapor	Water
$\rho$ (kg/m <sup>3</sup> )	0.59	958.05
$\mu$ (Pa)	$1.20 \times 10^{-5}$	$2.82 \times 10^{-4}$
$\lambda$ (W/mK)	$2.46 \times 10^{-2}$	$6.77 \times 10^{-1}$
$C_p$ (J/kgK)	2027	4216
$h_{\text{ig}}$ (J/kg)	$2.26 \times 10^6$	-
$\sigma$ (N/m)	$5.89 \times 10^{-2}$	-

thermophysical properties of water and water vapor are taken at saturation temperature and are given in Table 3. The bubble is placed in the center of the computational domain with sides of size  $L_x = L_y = L_z = 500 \mu\text{m}$ . The temperature and velocity fields are initialized using the analytical solution corresponding to  $Ro_0$ . We apply a constant pressure and zero heat flux boundary conditions to all walls. We consider four different grid sizes:  $\Delta x = 1, 0.625, 0.5,$  and  $0.4 \mu\text{m}$ , with the lowest resolution having three grid cells across the thermal boundary layer around the bubble.

## 4.2 | Results and discussion

Figure 8A shows a comparison between the evolution of the simulated bubble radius and the analytical solution from Equation 10. The simulated bubble radius approaches the analytical solution as the grid size is reduced. Furthermore, the temperature variation in radial direction at  $t = 28.22 \mu\text{s}$  is compared to the analytical solution from Equation 12 (Figure 8B). The temperature profile agrees well with the analytical solution and the bubble interface is strictly maintained at the saturation temperature indicating correct implementation of the sharp treatment of the energy equation.

Figure 9A shows the temperature distribution in the center plane at  $t = 28.22 \mu\text{s}$  for grid size  $\Delta x = 0.4 \mu\text{m}$ . The temperature distribution is spherically symmetric. A highly asymmetric temperature distribution was observed by Sato and Ničeno<sup>34</sup> for bubble growth simulations with similar configuration using the VOF method and this was attributed to the presence of artificial parasitic currents. These

parasitic currents are suppressed in the current simulations, because the LFRM method has an accurate surface tension calculation due to direct tracking of the interface, as indicated in the introduction. Figure 9B shows that a very small vortical velocity field is present inside the bubble which is of the order  $O(10^{-4})$  and about 0.04% of the interface velocity at  $t = 28.22 \mu\text{s}$ . Therefore, this deviation from the expected zero velocity in the bubble does not affect the temperature distribution in the thermal boundary layer surrounding the bubble.

## 5 | GROWTH OF A VAPOR BUBBLE IN A MICROCHANNEL

In this section, the simulation of the growth of a vapor bubble during flow boiling of water in a microchannel is presented. The results are compared to the simulation results given in Mukherjee and Kandlikar.<sup>11</sup>

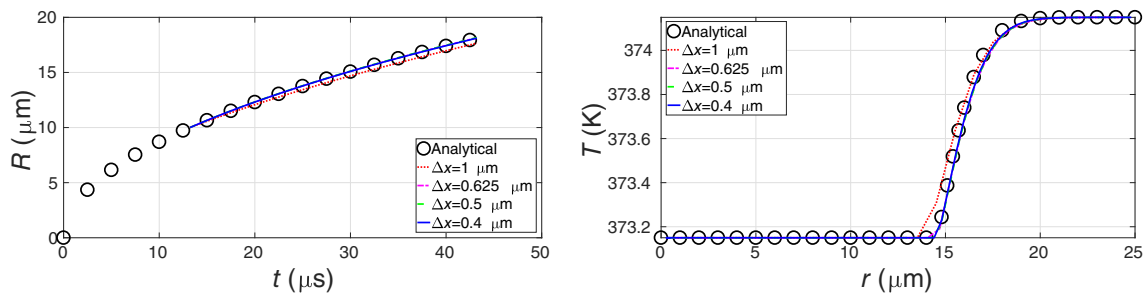
### 5.1 | Problem setup

The simulation parameters are taken from Mukherjee and Kandlikar.<sup>11</sup> A  $40 \mu\text{m}$  vapor bubble is initialized at  $(198, 99, 99) \mu\text{m}$  in a square channel of length  $L = 990 \mu\text{m}$  and width  $D = 198 \mu\text{m}$  as shown in Figure 10. The bubble is initially at saturation temperature  $T_{\text{sat}} = 373.15 \text{K}$ , whereas the surrounding water is at  $T_{\text{initial}} = 375.15 \text{K}$ . Water enters at a superheated temperature of  $T_{\text{in}} = 375.15 \text{K}$  with a velocity corresponding to  $Re = \rho_l D u_{\text{in}} / \mu_l = 100$ . No-slip and constant temperature  $T_w = 380.15 \text{K}$  boundary conditions are applied to all side walls. A constant pressure and a Neumann boundary condition for the temperature ( $dt/dn = 0$ ) are set at the outlet. All physical properties for water and water vapor are taken at  $373.15 \text{K}$ . The Bond number  $Bo = \rho_l g D^2 / \sigma = 0.0063$  for this simulation and hence gravity effects can be neglected. In this simulation, the grid size is taken as  $\Delta x = 1.98 \mu\text{m}$ , whereas the time step is set at  $\Delta t = 0.2 \mu\text{s}$ .

### 5.2 | Results and discussion

The growth of the vapor bubble in time is shown in Figure 11. Initially, the bubble grows while retaining its spherical shape and moves downstream in the direction of flow. Then, the bubble starts to elongate in the direction of flow, because the bubble has occupied almost the entire cross-section of the channel, which prevents further expansion in the  $y$ - $z$  plane.

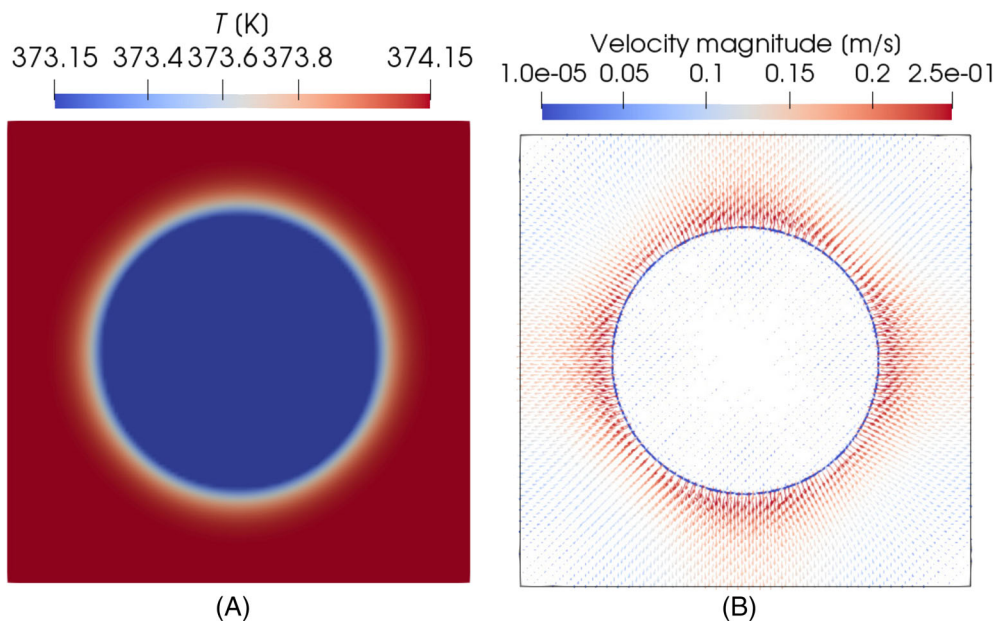
The numerical results obtained by LFRM qualitatively agree well with those reported by Mukherjee and Kandlikar<sup>11</sup> except for the last frame. In the study of Mukherjee and Kandlikar,<sup>11</sup> the bubble is seen to form a vapor patch at the wall. However, in case of LFRM, there is a liquid layer even though the bubble starts to become constrained by the walls. In the LS approach, as is used by Mukherjee and



(A) Evolution of bubble radius. (B) Temperature variation along the radial direction at  $t = 28.22 \mu\text{s}$ .

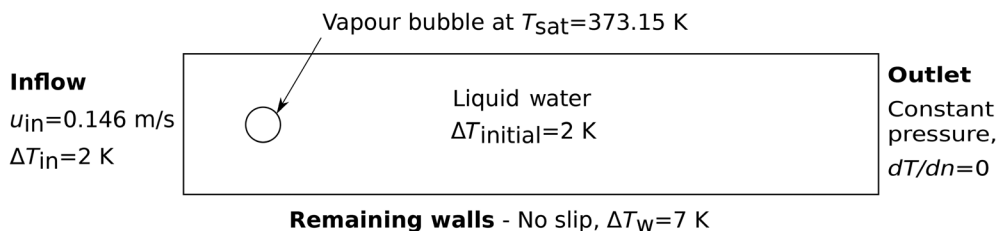
**FIGURE 8** Comparison of simulated bubble with the analytical solution for the bubble radius (A) and the temperature profile (B)

**FIGURE 9** Temperature (A) and velocity (B) distribution in the center plane at  $t = 28.22 \mu\text{s}$  for  $\Delta x = 0.4 \mu\text{m}$



(A) (B)

**FIGURE 10** Schematic of problem setup for vapor bubble growth in microchannel



Kandlikar,<sup>11</sup> such premature vapor patch formation is often obtained and is grid size dependent.<sup>10</sup>

In addition, there is a temporal lag that is caused by the different underlying assumptions in both methodologies. Mukherjee and Kandlikar<sup>11</sup> assumed the gas phase to remain at the imposed saturation temperature (even when the gas phase comes into direct contact with the superheated wall) and the interface velocity due to phase transition is weighed using the gas density only. On the other hand, in LFRM, the energy equation is also solved in the gas phase and a

harmonic average of gas and liquid density is used for the interface velocity, which reduces the overall interface velocity.

From the temperature distribution shown in Figure 12A, it can be seen that a thermal boundary is formed in the liquid near the wall. In addition, the bubble interface is accurately maintained at the saturation temperature even near the wall boundaries maintaining a sharp gradient in the temperature indicating a high heat transfer rate across the liquid film (which is one of the main causes of increased heat transfer in microchannel flow boiling). As shown in Figure 12B, the

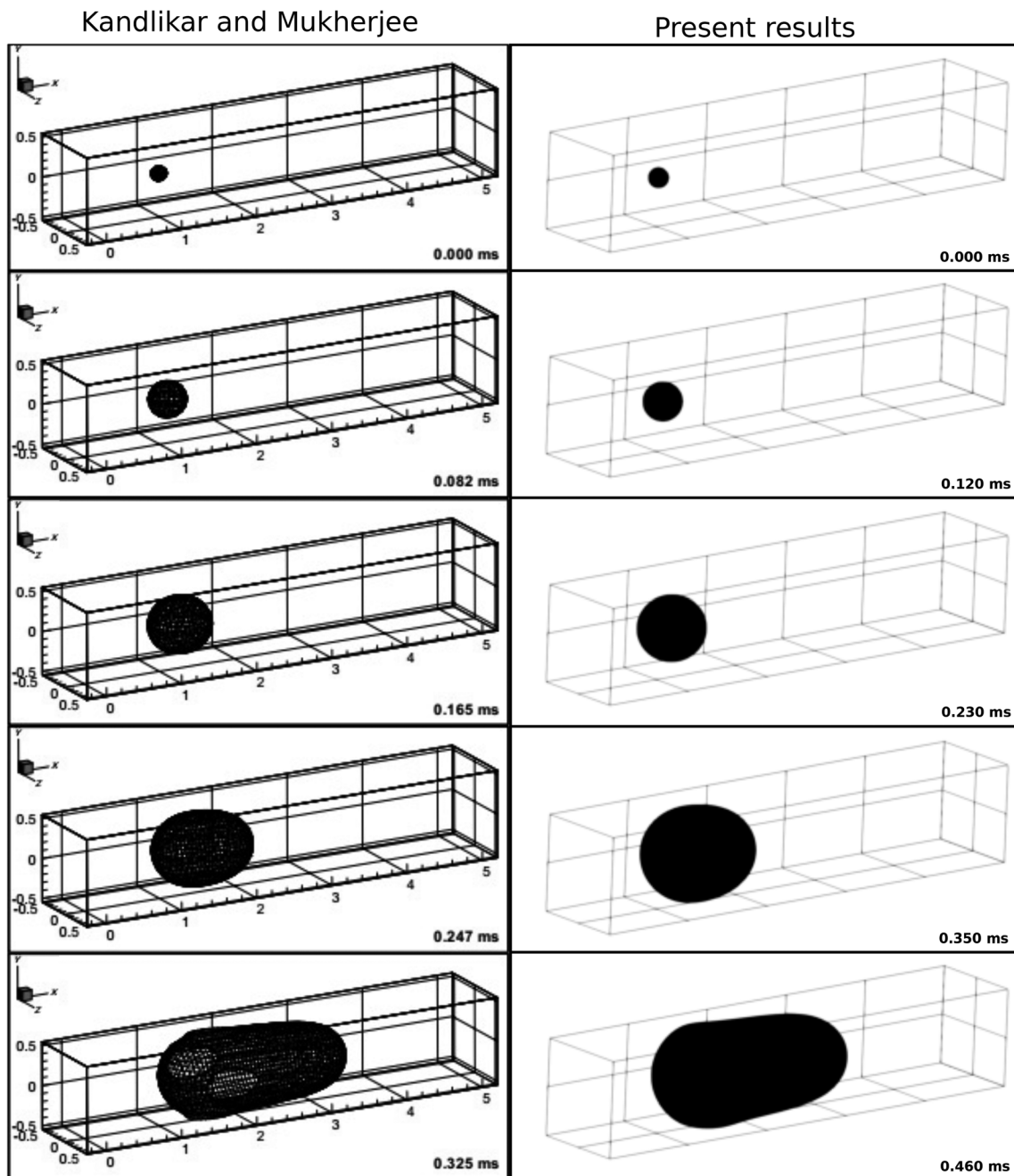


**FIGURE 11** Comparison of the bubble evolution from the current simulation (right) with the results from Kandlikar and Mukherjee<sup>11</sup> (left)

velocity is higher downstream of the bubble than upstream, indicating that as the bubble grows the liquid is pushed toward the outlet.

## 6 | PARAMETRIC STUDY

In this section, the effect of the wall temperature, inlet velocity, liquid mass density, and liquid heat capacity on the growth of a vapor bubble during microchannel flow boiling is studied. The studied system, channel dimensions, boundary conditions, and initial bubble size and temperature are kept the same as in the previous section. The grid cell size is selected similar to the previous section such that there exist at

least two cells across the thin liquid film. In this study, the domain is initialized with the steady state solution of the corresponding single phase flow and heat transfer problem, that is, with fully developed hydrodynamic and thermal profiles. For the base case, the fluid properties of water and water vapor, wall superheat of  $\Delta T = 8$  K and inlet Reynolds number  $Re = 100$  are selected.

### 6.1 | Results and discussion

A number of simulations are carried out using different parameters in order to study their influence on the equivalent bubble diameter, bubble

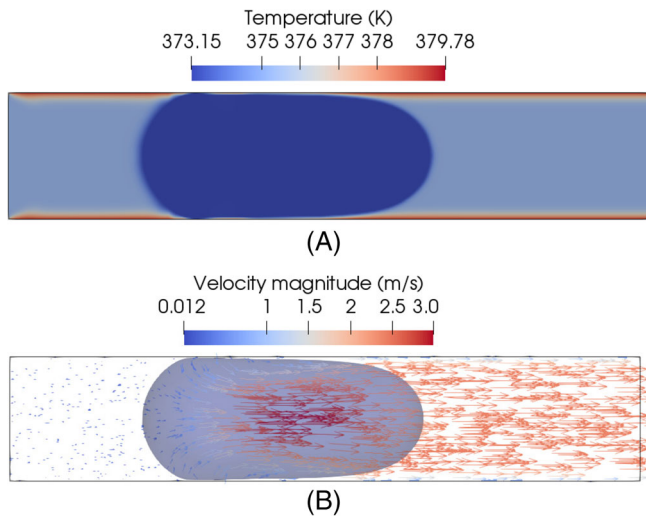


**FIGURE 12** Temperature (A) and velocity (B) distribution in the central vertical plane

upstream and downstream boundaries and dimensionless heat transfer rates from the wall (Nusselt number). The results are presented in non-dimensional units where the length and time scales are non-dimensionalized by the channel width ( $D = 198 \mu\text{m}$ ) and  $D/u_0$  ( $u_0$  corresponding to the given Reynolds number), respectively. The Nusselt number is defined as  $\text{Nu} = hD/\lambda_l$ , where  $h = -\lambda_l \frac{dT}{dn} / (T_w - T_{\text{sat}})$  is the heat transfer coefficient at the wall (calculated using heat flux normal to the wall) and  $\lambda_l$  is thermal conductivity of liquid. The dimensionless equivalent bubble diameter is defined as  $D_b = \frac{(6V_b/\pi)^{1/3}}{D}$  with  $V_b$  being net volume of the vapor bubble. It is important to note that our parametric study is performed for a specific system for a limited amount of time. Therefore, the trends obtained might not be universally applicable but still give a good indication of the influence of heat transfer parameters on flow boiling in microchannels.

## 6.2 | Effect of the wall temperature

The simulation results for three different wall superheats  $\Delta T = 5, 8,$  and  $10 \text{ K}$  are shown in Figure 13. Figure 13A shows that the initial growth of the bubble is similar until the bubble comes in contact with the thermal boundary layer near the wall (around  $D_b = 0.8$ ). Thereafter, the rate of bubble growth increases with increasing wall superheat.

In Figure 13B, the nondimensional downstream ( $L_1$ ) and upstream ( $L_2$ ) boundaries of the bubble are plotted as a function of time. The downstream end reaches the end of the channel faster with increasing wall superheat, indicating faster growth of the bubble slug. However, the wall superheat does not seem to influence the upstream part of the bubble. This is caused by the fact that the upstream end of the bubble moves with the imposed flow velocity,<sup>4</sup> which is the same for all three cases.

The time evolution of the Nusselt number (Figure 13C) indicates that the heat transfer from the walls increases as the bubble grows and interacts with the thermal boundary layer. As the thickness of the liquid film decreases, the thermal boundary layer becomes thinner,

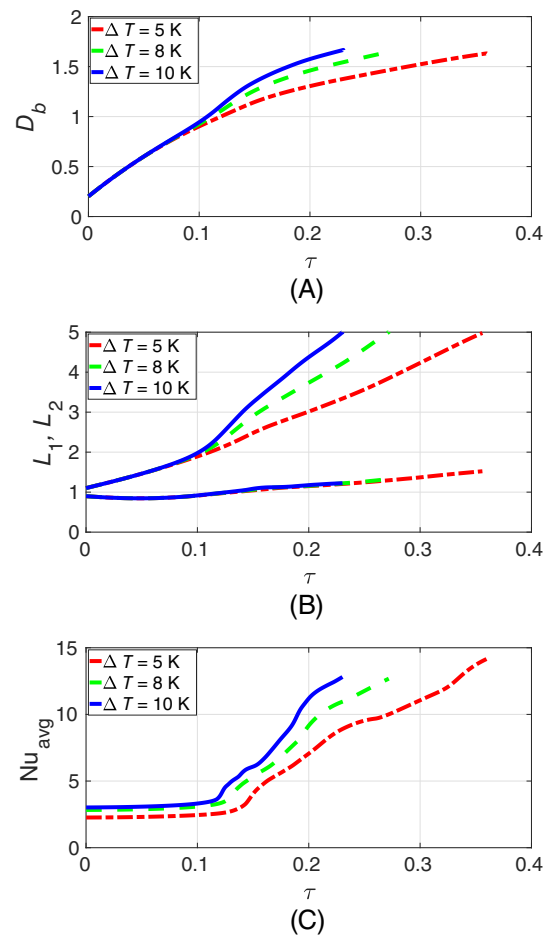


**FIGURE 13** Variation of (A) nondimensional equivalent diameter  $D_b$ , (B) nondimensional bubble cap locations  $L_1, L_2$ , and (C) average Nusselt number  $\text{Nu}_{\text{avg}}$  on bottom wall with nondimensional time  $\tau = tD/u_0$  for different wall temperatures

thereby increasing the heat transfer rate from the wall. With increased wall superheat, the driving temperature difference increases, leading to increased bubble growth rate. The increased bubble growth rate results in longer and thinner liquid film near the wall, thereby further increasing the net heat transfer rate from the wall.

## 6.3 | Effect of the inlet velocity

Simulations are carried out at three different Reynolds numbers ( $\text{Re} = 100, 200,$  and  $300$ ) by changing the fluid velocity. The results are shown in Figure 14. Figure 14A shows that the bubble growth rate decreases with increasing Reynolds number. The increased Reynolds number thins the thermal boundary at the wall, as seen in the initial temperature distribution in Figure 15. Therefore, the interaction of the bubble with the thermal boundary layer at the wall is delayed at high Reynolds number compared to low Reynolds number, which results in reduced bubble growth rate with increasing Reynolds number.

Figure 14B shows the relative importance of the convective transport of the bubble interface compared to the transport due to phase

change. As explained previously, the rapid bubble expansion through phase change, once it occupies the entire channel, leads to much faster transport of the bubble nose compared to the convective transport due to fluid flow, which is clearly visualized in Figure 16. The evolution of the bubble tail coincides for different Reynolds numbers, indicating that the tail travels with the average liquid inflow velocity.

From Figure 14C, it can be seen that the heat transfer rate from the wall is initially lower at low Reynolds number because of the relatively thick thermal boundary layer. However, the heat transfer rapidly increases once the bubble starts interacting with the wall thermal boundary. This shows an interesting interplay between convective heat transport and heat transfer due to phase change.

### 6.4 | Effect of the liquid mass density

Figure 17 shows the influence of changing the liquid mass density ( $\rho_l/\rho_g = 406, 812, \text{ and } 1624$ ) on the bubble growth. As the density ratio increases, more volume of vapor is generated for the same volume of evaporated liquid. This leads to a faster bubble growth rate as

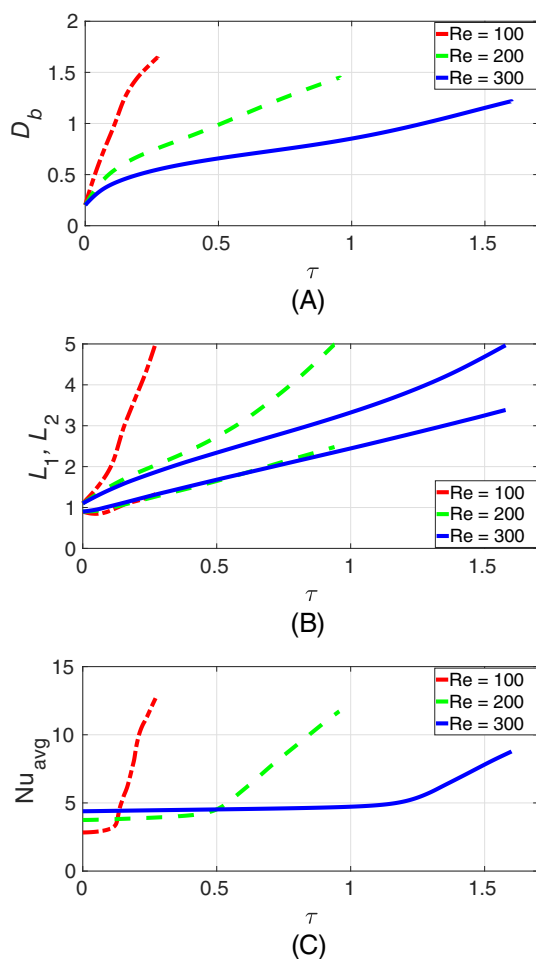


**FIGURE 14** Variation of (A) nondimensional equivalent diameter  $D_b$ , (B) nondimensional bubble cap locations  $L_1, L_2$ , and (C) average Nusselt number  $Nu_{avg}$  on bottom wall with nondimensional time  $\tau$  for different Reynolds numbers

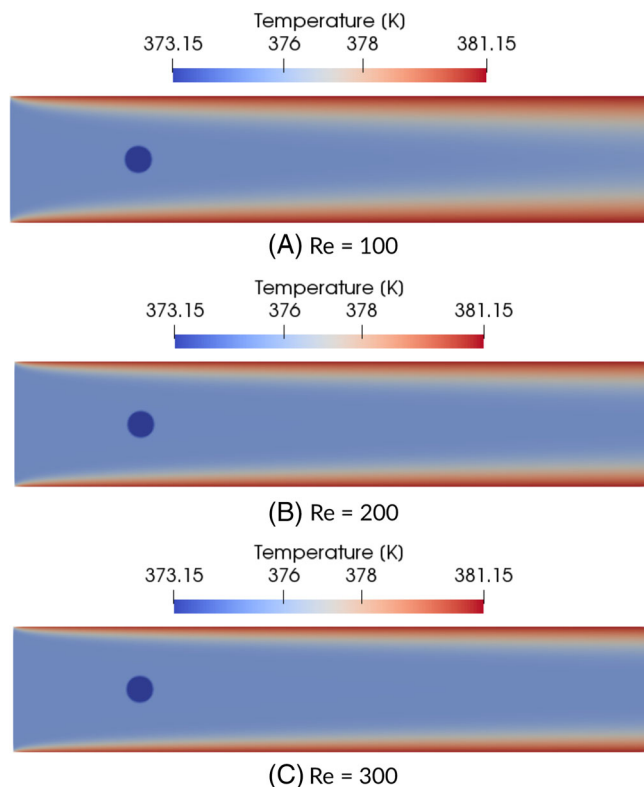


**FIGURE 15** Temperature distribution at the start of the simulation for different Reynolds numbers ( $Re = 100$  (A),  $Re = 200$  (B) and  $Re = 300$  (C))

shown in Figure 17A. The faster bubble growth rate leads to a faster transport of the bubble nose (Figure 17B). Again, it can be seen that the tail of the bubble travels mostly with the flow field and is hardly influenced by the growth of the boiling bubble. The higher bubble growth rate leads to a longer and thinner liquid film near the wall, resulting in an increased heat transfer rate from the wall (Figure 17C).

### 6.5 | Effect of the liquid heat capacity

Simulations are carried out at three liquid Prandtl numbers ( $Pr = \frac{c_p \mu_l}{\lambda_l} = 0.88, 1.76, \text{ and } 2.64$ ) by changing the heat capacity of the liquid, the results are shown in Figure 18. The bubble growth rate increases with an increase in the liquid heat capacity and thus with increasing Prandtl number (Figure 18A). This is inline with the analytical solution for homogeneous boiling whereby the bubble growth rate is typically proportional to square root of heat capacity.<sup>33</sup> In simple terms, the liquid with larger heat capacity will bring more heat at the vapor surface enabling more phase change.

## 7 | HEAT TRANSFER IN THE LIQUID FILM

The parametric study presented in the previous section showed that the average heat flux from the wall to the fluid is significantly

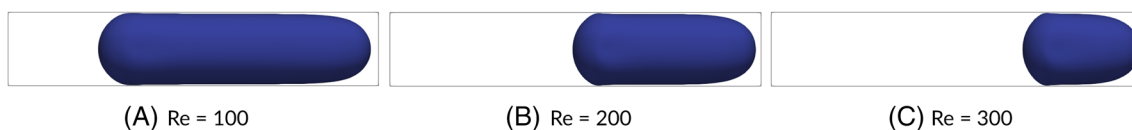


**FIGURE 16** Bubble shape at the end of the simulation for different Reynolds numbers ( $Re = 100$  (A),  $Re = 200$  (B) and  $Re = 300$  (C))

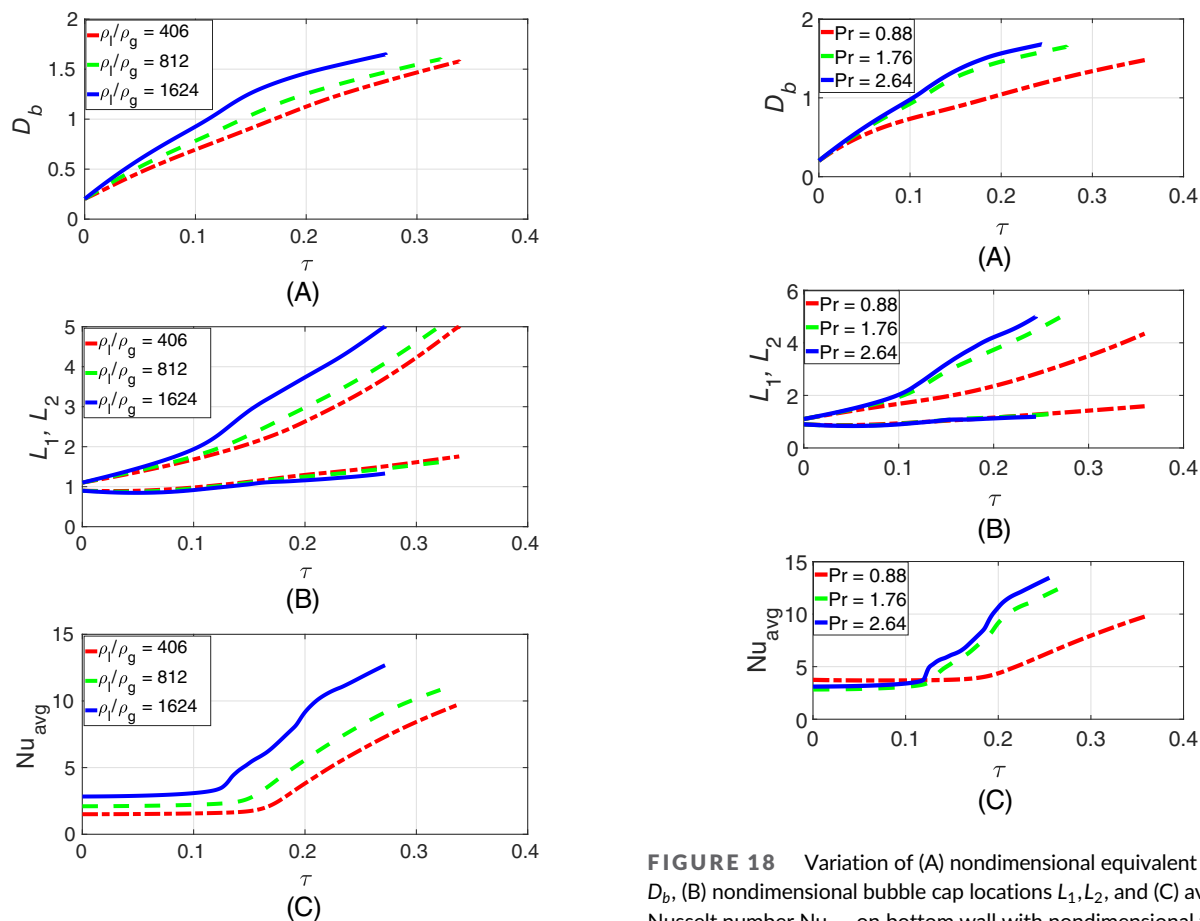


**FIGURE 17** Variation of (A) nondimensional equivalent diameter  $D_b$ , (B) nondimensional bubble cap locations  $L_1, L_2$ , and (C) average Nusselt number  $Nu_{avg}$  on bottom wall with nondimensional time  $\tau$  for different density ratios

augmented by the presence of the bubble. But because only the wall-averaged Nusselt number was considered, the spatial differences in the heat flux in relation to the bubble position and shape were left unaddressed. Therefore, in this section, we extend the analysis of the simulation results of the base case from the previous section, that is, with wall superheat of  $\Delta T = 8\text{ K}$  and inlet Reynolds number  $Re = 100$ , to provide more details on the heat transfer in the thin liquid film.

In Figure 19A, the bubble shape is shown for four different times, starting from a spherical bubble (at  $t = 0$  ms) which grows toward a vapor slug approaching the domain exit (at  $t = 0.36$  ms). The figure represents a cross-section at the central plane of the channel. Only the bottom-part of the channel is shown here, as the top and bottom

**FIGURE 18** Variation of (A) nondimensional equivalent diameter  $D_b$ , (B) nondimensional bubble cap locations  $L_1, L_2$ , and (C) average Nusselt number  $Nu_{avg}$  on bottom wall with nondimensional time  $\tau$  for different Prandtl numbers

solutions are symmetrical. Note that for clarity reasons, the figure is not up to scale; in reality, the channel length is five times the channel width.

The thickness of the liquid film under the bubbles ( $\delta$ ) is presented in dimensionless form in Figure 19B. For the largest bubble ( $t = 0.36$  ms), the average film thickness is approximately 5% of the channel half-width. It can be seen that the minimum of the film thickness occurs at the rear of the bubble at all times, as indicated by the triangles. The thinning of the film at the bubble rear is augmented by the transversal draining flows caused by the nonaxisymmetric bubble shape (Figure 20A), whereas the shape is symmetric at the front of the bubble (Figure 20C). The effects of the confinement make the liquid film thinner at the middle of the channel walls and thicker at the corners. This leads to build up of pressure gradient between the liquid at the channel walls and in the corners (Figure 20B), which gives rise



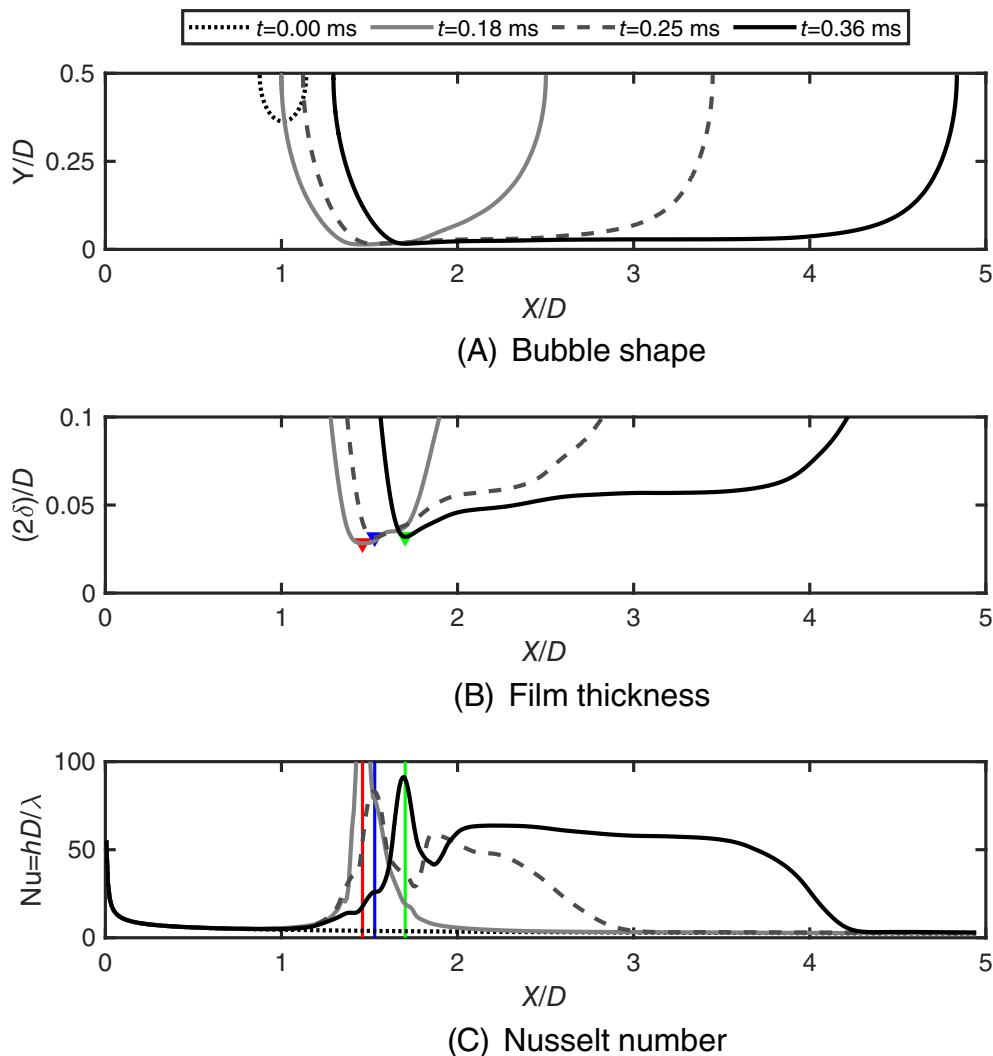


**FIGURE 19** Bubble shape (A), film thickness (B) and Nusselt number (c) evolution of a vapor bubble growing in a microchannel for base case

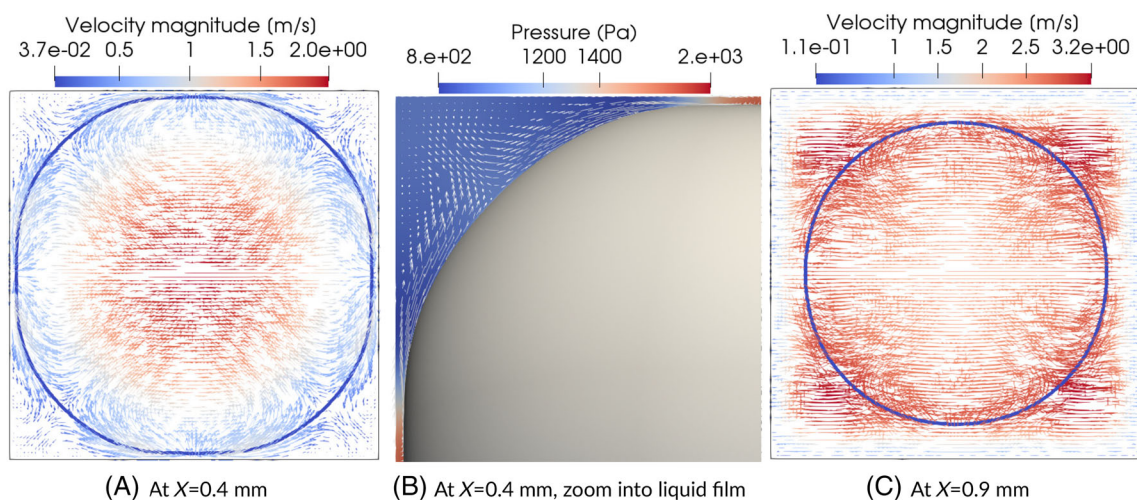


**FIGURE 20** Bubble shape and velocity distribution in the cross-sectional plane at different axial positions at time  $t = 0.36$  ms. Figure A shows the crosssectional plane at  $X = 0.4$  mm, figure B a zoom into the liquid film at  $X = 0.4$  mm and figure C the crosssectional plane at  $X = 0.9$  mm

to the draining flows. These draining flows push the liquid from the middle of the channel walls to the corners, further thinning the liquid film.

The local Nusselt number at the wall of the channel is shown in Figure 19C. At the channel entrance, the Nusselt number is high, but it quickly drops as the temperature profile in the liquid develops. At



the exit of the channel, the Nusselt number  $Nu_{\infty} = 2.97$  and is exactly equal to the analytical solution for fully developed laminar flow in a rectangular channel at constant wall temperature.<sup>35</sup> The Nusselt number at the bubble tail has a value higher than  $Nu_{\infty}$ . This shows that at the tail of the bubble the wall heat transfer rate is strongly affected by the presence of the bubble. The increase in heat transfer is likely

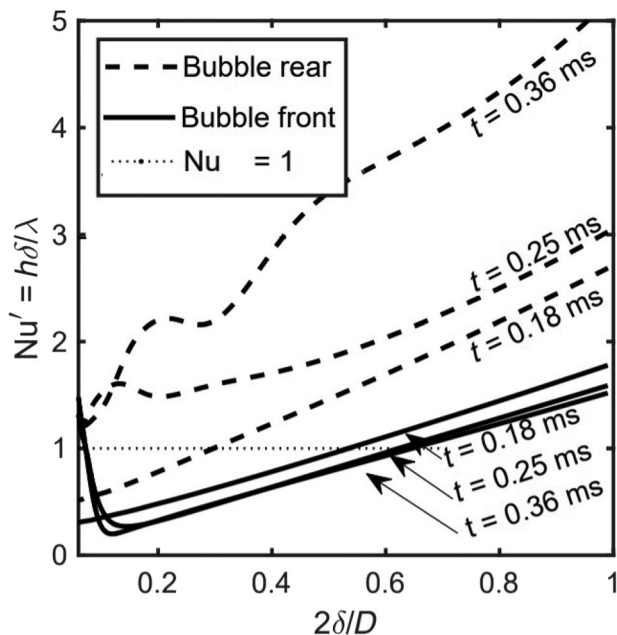


**FIGURE 21** Nusselt prime vs. film thickness, for the bubble shown in Figure 19 at different time instants, featuring the bubble rear and bubble front

caused by disruption of the developed velocity and temperature profiles by the bubble. On the contrary, the Nusselt number at the bubble nose is close to  $Nu_{\infty}$ . This shows that for the bubble nose, the wall heat transfer rate remains relatively unaffected by the presence of the bubble, as long as the vapor–liquid interface is far away from the wall.

Underneath the bubble Nusselt ranges from 60 to 150. By comparing the film thickness and Nusselt number graphs, it becomes clear that the highest Nusselt numbers are obtained at the positions where the gas–liquid interface is closest to the wall. This suggests that not convective heat transfer is the cause for these high Nusselt numbers, but rather phase change heat transfer, which scales with the thickness of the liquid film.

To verify this presumption, the Nusselt number was redefined by taking the liquid film thickness as the relevant length scale, resulting in an alternative Nusselt number ( $Nu' = h\delta/\lambda_L$ , aka “Nusselt prime”). In Figure 21, Nusselt prime is plotted vs. the liquid film thickness, for the base case at  $t = 0.18, 0.25,$  and  $0.36$  ms, corresponding to the bubble shapes shown previously in Figure 19. The film thickness is not uniquely defined, as the front and rear of the bubble might have the same thickness at different locations on the interface. Therefore, the front and the rear of the bubble are included as separate curves, which meet at the minimum film thickness location shown previously in Figure 19B. For reference, the Nusselt number for the 1D heat conduction limit is included, which is 1. Note that the graph for Nusselt prime does not show a “spike” for  $\delta$  going to zero, as was the case with the conventional Nusselt number. Instead, a gradual decrease in  $Nu'$  is seen with decreasing  $\delta$ . Note that the graph does not go entirely to zero but stops at  $(2\delta)/D = 0.08$ . Above this value, the liquid film spans at least four grid cells, which ensures reasonable calculation accuracy.

**FIGURE 22** Film thickness profiles for the largest bubble shape with the “flat film region” highlighted by blue region

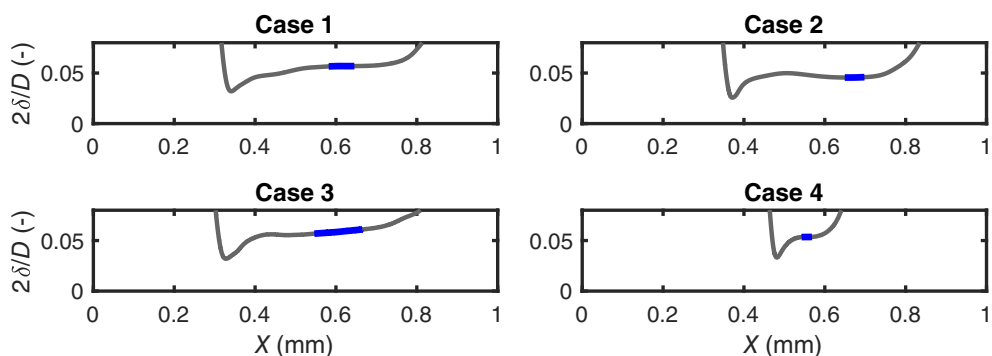


**TABLE 4** Dimensionless film thickness  $(2\delta_{num})/D$  and Nusselt number  $Nu'$  in the “flat film region,” based on the bubble sections indicated in Figure 22

Case	$\Delta T$ (K)	Re	$u_B$ (m/s)	$\frac{2\delta_{num}}{D}$	$(2\delta_{cal})/D$	$Nu'$
1	8	100	2.63	0.057	0.065	1.64
2	5	100	2.15	0.045	0.055	1.38
3	10	100	2.87	0.059	0.064	1.66
4	8	200	1.53	0.054	0.045	1.69

Note: The film thickness  $(2\delta_{cal})/D$  is calculated from correlation for parallel plates by Aussillous and Qu er .<sup>36</sup>

The bubble rear shows a higher  $Nu'$  for the same film thickness as compared to the bubble front. With decreasing film thickness,  $Nu'$  approaches a value towards 1 indicating that for thin films heat conduction becomes the dominant heat transfer mechanism. It is also observed that  $Nu' < 1$ , which might seem surprising at first. At the beginning, the small  $Nu'$  can be explained by the first interaction of the bubble with the boundary layer. However,  $Nu'$  is also found to be small in the rest of the simulation, primarily at the bubble nose. The low  $Nu'$  can be explained by a relatively low heat flux at the heated wall near the nose of the bubble because the liquid in front of the bubble is already at the superheated temperature. The heat flux will increase when the boundary layer of the heated wall and the bubble interact, because the temperature gradients are larger due to the boiling temperature at the gas-liquid interface.

As growth of the bubble takes place the bubble rear experiences an increase in the heat transfer rate (factor 2) from  $t = 18$  to  $t = 36$  ms. The bubble front remains nearly constant over time, showing a small decrease in the heat transfer rate ( $-14\%$ ) from  $t = 18$  to  $t = 36$  ms. Both the bubble rear and front curves in Figure 21 show some “wobbles,” which are caused by the curvature of the interface. In other words,  $Nu'$  changes when  $\delta \rightarrow 0$ , because the bubble rear becomes convex, while the bubble front becomes concave.

For elongated bubbles with phase change,  $\delta$  experiences some variation due to evaporation and volumetric expansion of the bubble, but in first approximation, this still leads to a relatively uniform film thickness over the entire bubble length. The region in which the film thickness is uniform is called the “flat film region.” The simulations shown in this study involve rather short bubbles ( $L/D < 4$ ), for which the film thickness does not attain a constant value. Nonetheless it is observed that in the final time-step of the simulations, the bubble is sufficiently elongated that a small but distinct “flat film region” could be observed (the blue line segment in Figure 22).

Based on the blue regions indicated in Figure 22, the film thickness  $(2\delta)/D$  and Nusselt number  $Nu'$  for the “flat film region” are calculated for different cases with different wall superheat and inlet Reynolds number (selected from previous section). As shown in Table 4, the film thickness in the “flat film region” ranges between 4% and 6% depending on the conditions at play, which is similar to an existing correlation for parallel plates by Aussillous and Quere,<sup>36</sup> which predicts the film thickness ranging from 4% to 7% for those same conditions.

The Nusselt number  $Nu'$  in the “flat film region” ranges from 1.38 to 1.69 (Table 4). If the temperature field in the thin film would be fully developed (no entrance effects),  $Nu'$  should be equal to unity, regardless of the specific velocity profile in the film. Since Nusselt numbers are larger than 1, this indicates that the temperature profile in the film is still developing. The velocity profile in the liquid film is parabolic as a result of the governing boundary conditions (no slip at the wall; near-free slip at the gas-liquid interface). Therefore this case bears resemblance to heat transfer in a laminar falling liquid film over a hot wall, for which several experimental studies exist that report Nusselt numbers of 1.06–1.72.<sup>37,38</sup> The higher Nusselt numbers (toward 1.72) are found for “wavy” film flow, where ripples lead to

periodic disruption of the thermal boundary layer. Overall the magnitude of Nusselt in a falling film is rather similar to our simulation results. From Table 4, it can be seen that  $Nu'$  increases with increasing wall superheat. This trend can be attributed to an increase in the volumetric growth rate of the bubble with increasing wall temperature. As the bubble grows faster in time, also the liquid film experiences a stronger acceleration and thus more convective heat transfer.

## 8 | CONCLUSION

In this article, we used the LFRM to study flow boiling in a microchannel. The hydrodynamics and heat transfer (including phase change) implementation of the current numerical model have been thoroughly verified and validated in our previous studies.<sup>23,24</sup> However, our model was not yet validated in the presence of walls. Therefore, the model is validated for the case of a Taylor bubble rising in a vertical tube in this article. The bubble terminal velocity and axial velocities at various locations are found in good agreement with the reference data sets.<sup>29–31</sup> We also presented the verification test case of the 3D bubble growth in supersaturated liquid using water-steam properties and successfully compare obtained results with the corresponding analytical solution.

The numerical simulation of growth of a single vapor bubble during flow boiling in a 200  $\mu\text{m}$  square microchannel is carried out. Once the bubble occupies the channel cross-section, an explosive growth of the bubble in the longitudinal direction is seen, because of a drastic increase in the heat transfer rate from the wall due to thin film evaporation. Because it is difficult to control the experimental settings, the results are compared with the data reported in the numerical study of Mukherjee and Kandlikar.<sup>11</sup> The obtained bubble evolution qualitatively agree well with these reference results, except for a temporal lag that is due to the difference in underlying assumptions in both methods. In addition, a premature vapor patch formation is seen in the reference results, which is not observed in the results obtained by LFRM.

Next, the influence of wall temperature, inlet velocity, liquid mass density, and liquid heat capacity on bubble growth rate and heat transfer rate in microchannel flow boiling has been quantified. The bubble growth rate and the net heat transfer rate from the wall increase with increasing wall superheat indicating the importance of conductive heat transport in the thin liquid film between the bubble and the wall. On the other hand, increasing the inlet velocity decreases the bubble growth rate and the net heat transfer rate in spite of the increase in the convective heat transfer indicating the importance of phase change on overall heat transfer from the wall. As expected, the bubble growth rate and the net heat transfer rate increase with liquid mass density and liquid heat capacity.

Finally, the heat transfer in the liquid film is studied. It is observed that the minima of the film thickness is always located at the rear of the bubble due to the transversal draining flows. It is shown that the heat transfer rate between the bubble interface and the channel wall is inversely proportional to the distance between them. This

demonstrates that the liquid film thickness is a more relevant choice of length scale for the Nusselt number compared to the channel width. In the “flat film region,” this alternative Nusselt number is found similar to the Nusselt number for falling films. At the bubble rear, the convective effects are most pronounced, whereas the heat transfer at the bubble front remains relatively unaffected by the presence of the bubble.

It should be noted that in this article, the resolution in the liquid film is in some parts of the simulations only two grid cells. This will of course lead to grid-dependent results. Although these parts are not included in the quantitative comparison of the results, future research should focus on obtaining grid-independent results. Currently this is not possible, due to the high computational requirements of these simulations for higher resolutions.

### ACKNOWLEDGMENTS

This study is part of the research programme Open Technologieprogramma with project number 13781, which is (partly) financed by the Netherlands Organisation for Scientific Research (NWO) Domain Applied and Engineering Sciences (TTW, previously Technology Foundation STW). The numerical simulations were carried out on the Dutch national e-infrastructure with the support of SURF Cooperative.

### AUTHOR CONTRIBUTIONS

**Adnan H. Rajkotwala:** Data curation (equal); formal analysis (equal); investigation (equal); methodology (equal); software (equal); writing – original draft (equal). **Leander L Boer:** Formal analysis (equal); investigation (equal); writing – original draft (equal). **E. A. J. F. (Frank) Peters:** Conceptualization (equal); formal analysis (equal); methodology (equal); software (equal); supervision (equal); writing – review and editing (equal). **Cees W. M. van der Geld:** Conceptualization (equal); formal analysis (equal); funding acquisition (equal); project administration (equal); supervision (equal); writing – review and editing (equal). **J. G. M. (Hans) Kuerten:** Conceptualization (equal); formal analysis (equal); funding acquisition (equal); project administration (equal); supervision (equal); writing – review and editing (equal). **J. A. M. (Hans) Kuipers:** Conceptualization (equal); formal analysis (equal); funding acquisition (equal); methodology (equal); project administration (equal); software (equal); supervision (equal); writing – review and editing (equal). **Maike W. Baltussen:** Conceptualization (equal); formal analysis (equal); investigation (equal); methodology (equal); software (equal); supervision (equal); writing – original draft (supporting); writing – review and editing (equal).

### DATA AVAILABILITY STATEMENT

The data that support the findings of this study are available from the corresponding author upon reasonable request.

### ORCID

E. A. J. F. (Frank) Peters  <https://orcid.org/0000-0001-6099-3583>

Maike W. Baltussen  <https://orcid.org/0000-0003-4265-9164>

### REFERENCES

1. Karayiannis TG, Mahmoud MM. Flow boiling in microchannels: fundamentals and applications. *Appl Therm Eng.* 2017;115:1372-1397.
2. Agostini B, Fabbri M, Park JE, Wojtan L, Thome JR, Michel B. State of the art of high heat flux cooling technologies. *Heat Transf Eng.* 2007; 28(4):258-281. doi:10.1080/01457630601117799
3. Magnini M, Thome JR. A CFD study of the parameters influencing heat transfer in microchannel slug flow boiling. *Int J Therm Sci.* 2016; 110:119-136.
4. Magnini M, Pulvirenti B, Thome JR. Numerical investigation of hydrodynamics and heat transfer of elongated bubbles during flow boiling in a microchannel. *Int J Heat Mass Transf.* 2013;59:451-471.
5. Szczukiewicz S, Magnini M, Thome JR. Proposed models, ongoing experiments, and latest numerical simulations of microchannel two-phase flow boiling. *Int J Multiphase Flow.* 2014;59:84-101.
6. Thome JR. Boiling in microchannels: a review of experiment and theory. *Int J Heat Fluid Flow.* 2004;25(2):128-139.
7. Kandlikar SG. History, advances, and challenges in liquid flow and flow boiling heat transfer in microchannels: a critical review. *J Heat Transf.* 2012;134(3):034001. doi:10.1115/1.4005126
8. Tibirić CB, Ribatski G. Flow boiling in micro-scale channels - synthesized literature review. *Int J Refrig.* 2013;36(2):301-324.
9. Baldassari C, Marengo M. Flow boiling in microchannels and microgravity. *Prog Energy Combust Sci.* 2013;39(1):1-36.
10. Guo Z, Fletcher DF, Haynes BS. A review of computational modelling of flow boiling in microchannels. *J Comput Multiph Flows.* 2014;6(2): 79-110. doi:10.1260/1757-482X.6.2.79
11. Mukherjee A, Kandlikar SG. Numerical simulation of growth of a vapor bubble during flow boiling of water in a microchannel. *Microfluid Nanofluid.* 2005;1:137-145.
12. Mukherjee A, Kandlikar SG, Edel ZJ. Numerical study of bubble growth and wall heat transfer during flow boiling in a microchannel. *Int J Heat Mass Transf.* 2011;54(15-16):3702-3718.
13. Lee W, Son G. Bubble dynamics and heat transfer during nucleate boiling in a microchannel. *Numer Heat Transf Part A Appl.* 2008; 53(10):1074-1090. doi:10.1080/10407780701789898
14. Zu YQ, Yan YY, Gedupudi S, Karayiannis TG, Kenning DBR. Confined bubble growth during flow boiling in a mini-/micro-channel of rectangular cross-section part II: approximate 3-D numerical simulation. *Int J Therm Sci.* 2011;50(3):267-273.
15. Zhuan R, Wang W. Flow pattern of boiling in micro-channel by numerical simulation. *Int J Heat Mass Transf.* 2012;55(5-6):1741-1753.
16. Magnini M, Pulvirenti B, Thome JR. Numerical investigation of the influence of leading and sequential bubbles on slug flow boiling within a microchannel. *Int J Therm Sci.* 2013;71:36-52.
17. Magnini M, Thome JR. Use of two-phase CFD simulations to develop a boiling heat transfer prediction method for slug flow within microchannels. International Electronic Packaging Technical Conference and Exhibition. 2015;56901:V003T10A020. doi: 10.1115/IPACK2015-48033
18. Jacobi AM, Thome JR. Heat transfer model for evaporation of elongated bubble flows in microchannels. *J Heat Transf.* 2002;124(6): 1131-1136. doi:10.1115/1.1517274
19. Ferrari A, Magnini M, Thome JR. Numerical analysis of slug flow boiling in square microchannels. *Int J Heat Mass Transf.* 2018;123: 928-944.
20. Shin S, Yoon I, Juric D. The local front reconstruction method for direct simulation of two- and three-dimensional multiphase flows. *J Comput Phys.* 2011;230(17):6605-6646.
21. Dijkhuizen W, Roghair I, van Sint AM, Kuipers JAM. DNS of gas bubbles behaviour using an improved 3D front tracking model - model development. *Chem Eng Sci.* 2010;65(4):1427-1437.

22. Baltussen MW, Kuipers JAM, Deen NG. A critical comparison of surface tension models for the volume of fluid method. *Chem Eng Sci.* 2014;109:65-74.
23. Rajkotwala AH, Mirsandi H, Peters EAJF, et al. Extension of local front reconstruction method with controlled coalescence model. *Phys Fluids.* 2018;30(2):022102. doi:10.1063/1.5008371
24. Rajkotwala AH, Panda A, Peters EAJF, et al. A critical comparison of smooth and sharp interface methods for phase transition. *Int J Multiphase Flow.* 2019;120:103093.
25. Shin S, Abdel Khalik SI, Daru V, Juric D. Accurate representation of surface tension using the level contour reconstruction method. *J Comput Phys.* 2005;203(2):493-516. doi:10.1016/j.jcp.2004.09.003
26. Mirsandi H, Rajkotwala AH, Baltussen MW, Peters EAJF, Kuipers JAM. Numerical simulation of bubble formation with a moving contact line using local front reconstruction method. *Chem Eng Sci.* 2018;187:415-431.
27. Das S, Deen NG, Kuipers JAM. Direct numerical simulation for flow and heat transfer through random open-cell solid foams: development of an IBM based CFD model. *Catal Today.* 2016;273:140-150.
28. Udaykumar HS, Shyy W, Rao MM. Elafint: a mixed Eulerian-Lagrangian method for fluid flows with complex and moving boundaries. *Int J Numer Methods Fluids.* 1996;22:691-712.
29. Bugg JD, Saad GA. The velocity field around a Taylor bubble rising in a stagnant viscous fluid: numerical and experimental results. *Int J Multiphase Flow.* 2002;28(5):791-803.
30. Ndinisa NV, Wiley DE, Fletcher DF. Computational fluid dynamics simulations of Taylor bubbles in tubular membranes: model validation and application to laminar flow systems. *Chem Eng Res Des.* 2005; 83(1):40-49.
31. Gutiérrez E, Balcázar N, Bartrons E, Rigola J. Numerical study of Taylor bubbles rising in a stagnant liquid using a level-set/moving-mesh method. *Chem Eng Sci.* 2017;164:158-177.
32. Deen NG, Kriebitzsch SHL, van der Hoef MA, Kuipers JAM. Direct numerical simulation of flow and heat transfer in dense fluid-particle systems. *Chem Eng Sci.* 2012;81:329-344.
33. Scriven LE. On the dynamics of phase growth. *Chem Eng Sci.* 1995; 50(24):3905.
34. Sato Y, Ničeno B. A sharp-interface phase change model for a mass-conservative interface tracking method. *J Comput Phys.* 2013;249: 127-161. doi:10.1016/j.jcp.2013.04.035
35. Shah RK, London AL. Chapter VII - rectangular ducts. In: Shah RK, London AL, eds. *Laminar Flow Forced Convection in Ducts.* Academic Press; 1978:196-222.
36. Aussillous P, Quéré D. Quick deposition of a fluid on the wall of a tube. *Phys Fluids.* 2000;12(10):2367-2371. doi:10.1063/1.1289396
37. Faghri A, Zhang Y. 9 - Evaporation. In: Faghri A, Zhang Y, eds. *Transport Phenomena in Multiphase Systems Boston.* Academic Press; 2006:678-764.
38. Soo Too YC, Morrison G, Behnia M. Falling film heat exchangers for solar water heaters. ANZSES Annual Conference Canberra. 2006, 01.

**How to cite this article:** Rajkotwala AH, Boer LL, Peters E(F), et al. A numerical study of flow boiling in a microchannel using the local front reconstruction method. *AIChE J.* 2022;68(4): e17598. doi:10.1002/aic.17598